FULL PAPER

Zn–Co Batteries

ADVANCED
FUNCTIONAL
MATERIALS

www.afm-journal.d

Finely Crafted 3D Electrodes for Dendrite-Free and High-Performance Flexible Fiber-Shaped Zn–Co Batteries

Ming Li, Jiashen Meng, Qi Li,* Meng Huang, Xiong Liu, Kwadwo Asare Owusu, Ziang Liu, and Liqiang Mai*

Rechargeable aqueous Zn-based batteries, benefiting from their good reliability, low cost, high energy/power densities, and ecofriendliness, show great potential in energy storage systems. However, the poor cycling performance due to the formation of Zn dendrites greatly hinders their practical applications. In this work, a trilayer 3D CC-ZnO@C-Zn anode is obtained by in situ growing ZIFs (zeolitic-imidazolate frameworks) derived ZnO@C core–shell nanorods on carbon cloth followed by Zn deposition, which exhibits excellent antidendrite performance. Using CC-ZnO@C-Zn as the anode and a branch-like $Co(CO_3)_{0.5}(OH)_x \cdot 0.11H_2O@CoMoO_4$ (CC-CCH@CMO) as the cathode, a Zn–Co battery is rationally designed, displaying excellent energy/power densities (235 Wh kg^{-1}, 12.6 kW kg^{-1}) and remarkable cycling performance (71.1% after 5000 cycles). Impressively, when using a gel electrolyte, a highly customizable, fiber-shaped flexible all-solid-state Zn–Co battery is assembled for the first time, which presents a high energy density of 4.6 mWh cm^{-3}, peak power density of 0.42 W cm^{-3}, and long durability (82% capacity retention after 1600 cycles) as well as excellent flexibility. The unique 3D electrode design in this study provides a novel approach to achieve high-performance Zn-based batteries, showing promising applications in flexible and portable energy-storage systems.

1. Introduction

With ever-worsening environmental conditions and the overwhelming demand for renewable energy, as well as the ever-growing pursuit of portable electronics, the flexible and wearable energy storage devices with high energy/power density, long durability, low cost, and good safety are receiving increasing attention.[1] In the past decades, considerable efforts have been made to the development of flexible alkali metal ion batteries (Li$^+$, Na$^+$, K$^+$) due to their high energy densities.[2] However, a series of intrinsic issues of alkali metal ion batteries, such as the rising price of lithium/sodium/potassium, toxicity and flammability of organic electrolytes, significantly restrict their wide applications, especially for the wearable electronics that may be exposed to the skin (such as epidermal sensors).[3] Flexible supercapacitors that traditionally use aqueous electrolytes have been considered as potential alternatives to flexible alkali metal ion batteries due to the good safety and being cost effective,[4] but their relatively low energy densities are far from being satisfactory for more extensive applications.[5]

Exhilaratingly, Zn-based batteries, due to their unique advantages of high output voltage, high theoretical capacity of Zn (825 mAh g^{-1}), ecofriendliness and low cost, are considered as strong candidates to solve the dilemma of energy storage between alkali metal ion batteries and supercapacitors.[6] The aqueous electrolytes used can provide higher ionic conductivity and better safety than organic electrolytes, therefore resulting in a much higher rate performance.[7] However, two key issues seriously hinder their wide applications. One is the formation and growth of Zn dendrites which greatly shorten the cycling life of the Zn-based battery (usually less than 500 cycles).[8] The other is the use of heavy Zn plate (around 750 mg cm^{-2}) as the anode in conventional Zn-based batteries,[9] which decreases the energy density and also limits their applications in flexible energy storage devices. In order to address the aforementioned issues, tremendous efforts have been devoted to designing flexible Zn-based anodes via strategies including nanostructure design and hybrid materials.[10] For example, Liu et al.[11] reported a flexible Ni–Zn battery based on a hierarchical ZnO/carbon nanofiber anode, and achieved good energy/power densities of 323.3 Wh kg^{-1}, 8.66 kW kg^{-1} based on active materials. However, the capacity retention of ≈ 72.9% after 2400 cycles is not satisfactory. Wang et al.[12] developed a novel Ni–Zn battery by using La$_2$O$_3$-doped ZnO as the anode. Although this doping strategy results in enhanced battery performances compared to ZnO anodes, the lack of flexibility restricts its further application in the flexible energy storage systems. Furthermore, a great deal of the flexible batteries with the geometrical restrictions of two dimension (2D), are difficult to meet the practical applications for small wearable devices. Hence, the search for feasible approaches to fabricate cost-effective, dendrite-free, high security, flexible Zn-based batteries is highly desired.

Dr. M. Li, Dr. J. S. Meng, Prof. Q. Li, Dr. M. Huang, Dr. X. Liu,
Dr. K. A. Owusu, Dr. Z. Liu, Prof. L. Q. Mai
State Key Laboratory of Advanced Technology for Materials Synthesis
and Processing
Wuhan University of Technology
Hubei, Wuhan 430070, P. R. China
E-mail: qi.li@whut.edu.cn; mlq518@whut.edu.cn

Herein, a new type of Zn-based (Zn–Co) battery was assembled for the first time based on finely crafted 3D flexible electrodes, delivering an ultrastable cycling performance (71.1% after 5000 cycles) and outstanding energy/power densities of 235 Wh kg^{-1} and 12.6 kW kg^{-1} based on the active materials on both electrodes. A trilayer CC-ZnO@C-Zn as the anode was obtained by in situ growing ZIF-8 (zeolitic-imidazolate frameworks) derived ZnO@C core–shell nanorods as the skeleton on carbon cloth (CC) followed by Zn deposition, which shows excellent antidendrite performance due to the unique 3D skeleton matrix. Hierarchical branch-like Co(CO$_3$)$_{0.5}$(OH)$_x$·0.11H$_2$O@ CoMoO$_4$ grown on CC (CC-CCH@CMO) was used as the cathode, exhibiting a high areal capacity of 0.72 mAh cm^{-2}. Since the active materials were grown on soft CC (only 13 mg cm^{-2}) and then directly used as 3D binder-free electrodes, it ensures the electrode flexibility and also enables the fast electron transfer diffusion. Importantly, an all-solid-state flexible fiber-shaped Zn–Co battery, using the polyvinyl alcohol (PVA)–KOH gel electrolyte, was constructed for the first time. As a consequence, it achieved a considerable capacity of 3 mAh cm^{-3} with superior energy/power densities (4.6 mWh cm^{-3}, 0.42 W cm^{-3}) and exhibited well-maintained battery performances under various bending tests, superior than most of other reported flexible energy storage devices. Furthermore, the fiber shape of our Zn–Co battery enables it to be easily customized for portable electronics. As a demonstration, a flexible device assembled by three batteries in series was successfully used to power a series of light emitting diodes (LEDs), a smartphone and a bracelet digital watch. Hence, this work provides a novel approach to fabricate dendrite-free fiber-shaped Zn–Co battery with high-performance and flexibility, which paves the path for the development of flexible energy storage devices.

2. Results and Discussion

2.1. Morphology and Structure Characterization

The schematic diagram of the aqueous Zn–Co full battery and the redox reactions during charge–discharge processes are illustrated in **Scheme 1**. The integrated trilayer CC-ZnO@C-Zn anode was synthesized by a three-step process (Figure S1, Supporting Information). Initially, the ZnO nanorods were in situ grown on the flexible carbon cloth by a facile low-temperature hydrothermal process to form CC-ZnO. The X-ray diffraction (XRD) pattern (Figure S2a, Supporting Information) demonstrates that the characteristic peaks are well indexed to ZnO (JCPDS card No.079-0206) except the ones originating from the CC. Next, the ZIF shell was formed on the surface of ZnO nanorods via a low-pressure vapor superassembly[13] followed by the heat treatment in N$_2$ atmosphere to obtain carbon coated CC-ZnO@C skeletons. According to the XRD patterns (Figure S2b, Supporting Information) and Fourier transform infrared (FT-IR) spectra (Figure S2c, Supporting Information), the typical peaks of ZIF shell are clearly distinguished.[14] Finally, the finely designed 3D CC-ZnO@C skeleton was subjected to a Zn deposition procedure to obtain the antidendrite anode (CC-ZnO@C-Zn). On the other hand, the CC-CCH@ CMO cathode was synthesized by a two-step hydrothermal process. As the schematic illustration shows in Figure S3 (Supporting Information), the CCH nanowires were first grown on CC directly, and followed by homogeneously growing CoMoO$_4$ nanosheets on the surface of CCH nanowires to form the 3D branch-like nanostructure. The optical photograph of the as-synthesized electrodes demonstrates an even distribution of the electrode materials on CC (Figure S4, Supporting Information).

As shown in **Figure 1**a–c, ZnO nanorods are coated with a rough layer of ZIF-derived carbon with the thickness of 20–50 nm (Figure 1d and the inset picture) to form the core-shell structured CC-ZnO@C. The uncoated ZnO nanorods are shown in Figure S5a–c (Supporting Information). As displayed in Figure 1e, numerous tiny ZnO nanodots are embedded in the porous carbon layer. Its lattice spacing of 0.26 nm corresponds well to the (002) plane of ZnO (Figure 1f). The well-maintained hierarchical structure of the ZIF-derived carbon nanotubes (Figure S6, Supporting Information) which were obtained by removing the ZnO core with HCl solution indicates the existence of carbon and the strong adhesion of the active materials to the CC substrate even without any binder. The phase and composition of CC-ZnO@C skeletons were
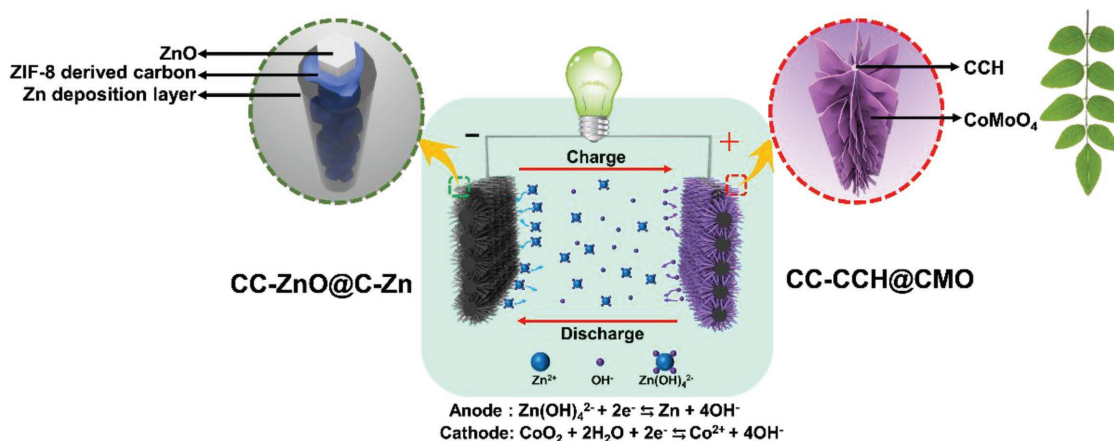
Scheme 1. Schematic illustration of the Zn–Co full battery using the finely crafted 3D CC-ZnO@C-Zn anode and CC-CCH@CMO cathode, together with the redox reactions during charge–discharge processes.
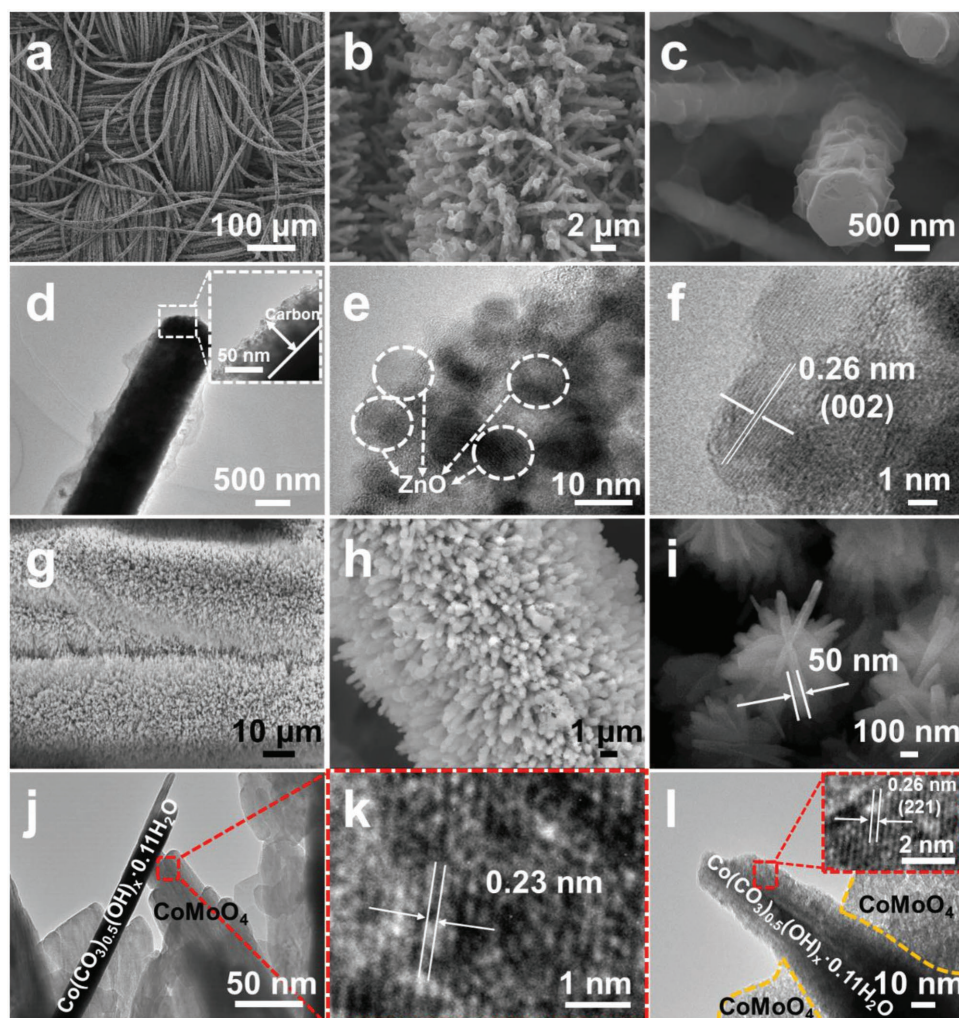
ADVANCED
SCIENCE NEWS
www.advancedsciencenews.com

ADVANCED
FUNCTIONAL
MATERIALS
www.afm-journal.de

Figure 1. a–c) SEM, d–f) TEM and HRTEM images of core/shell CC-ZnO@C skeletons with the inset in (d) representing the high-magnification TEM image of a selected area. g–i) SEM, j–l) TEM and HRTEM images of branch-like CC-CCH@CMO with the inset in (l) representing the HRTEM image of a selected area.

further investigated by X-ray photoelectron spectroscopy (XPS). Figure S7a (Supporting Information) reveals the presence of Zn, O, N, and C elements, which is consistent with the energy-dispersive X-ray spectroscopy (EDS) elemental mapping results (Figure S8, Supporting Information). The two peaks (Figure S7b, Supporting Information) located at 1021.78 and 1044.78 eV correspond to Zn $2p_{3/2}$ and Zn $2p_{1/2}$ respectively, which agrees well with the literature reports for ZnO.[15] The high-resolution N 1s spectrum (Figure S7c, Supporting Information) can be deconvoluted into pyridinic N (398.8 eV), pyrrolic N (400.1 eV), and graphitic N (401.6 eV), confirming the nitrogen doping in the ZIF-derived carbon shell.[16] Moreover, two broad peaks in the Raman spectrum (Figure S9, Supporting Information) located at around 1349 and 1585 cm^{-1} are assigned to the D (disordered carbon) and G (graphitic carbon) bands respectively, with the calculated I_D/I_G values of 1.22 and 0.91 for the CC-ZnO@C and CC-ZnO samples, further indicating the partly graphitized nature of the carbon shell.[17]

As shown in Figure 1g–i, the branch-like CC-CCH@CMO materials which are composed of $Co(CO_3)_{0.5}(OH)_x \cdot 0.11H_2O$

nanowires (CCH) and $CoMoO_4$ nanosheets were uniformly grown on the CC. The CCH nanowires grown on CC were shown in Figure S5d–f (Supporting Information). The lattice spacing of 0.23 nm in Figure 1j,k corresponds well to the XRD peak of $CoMoO_4$ located at 39° (JCPDS card No.015-0439). The characteristic peaks of the XRD pattern for the CC-CCH (Figure S10a, Supporting Information) are well indexed to $Co(CO_3)_{0.5}(OH)_x \cdot 0.11H_2O$ (JCPDS card No.048-0083) with the lattice spacing of 0.26 nm well corresponding to its (221) plane (Figure 1l and inset). However, the typical peaks of the low-crystalline $Co(CO_3)_{0.5}(OH)_x \cdot 0.11H_2O$ in the CC-CCH@ CMO sample are not obvious and concealed by the $CoMoO_4$ patterns (Figure S10b, Supporting Information). In order to prove the dual composition, the $Co(CO_3)_{0.5}(OH)_x \cdot 0.11H_2O$ was transformed to high-crystalline Co_3O_4 (300 °C in air for 2 h). Two groups of characteristic peaks for Co_3O_4 and $CoMoO_4$ are observed in the XRD pattern (Figure S10c, Supporting Information) of the obtained sample, indicating two different phases existing in this sample. The XPS and the elemental mapping images (Figures S10d and S11, Supporting Information) show

ADVANCED
SCIENCE NEWS
www.advancedsciencenews.com

ADVANCED
FUNCTIONAL
MATERIALS
www.afm-journal.de

the presence and even distribution of Co, O, and Mo elements in CC-CCH@CMO. In its further XPS analyses, the two peaks of the Mo 3d spectrum located at 235.0 and 231.9 eV are consistent well with the Mo^{6+} species, confirming the presence of CoMoO$_4$ (Figure S10e, Supporting Information).[18] The Co 2p spectrum contains two core-level peaks of Co 2p$_{1/2}$ (795.9 eV) and Co 2p$_{3/2}$ (779.5 eV) as well as two small satellite peaks, which can be assigned to Co(CO$_3$)$_{0.5}$(OH)$_x$·0.11H$_2$O and CoMoO$_4$, respectively (Figure S10f, Supporting Information), also proving the presence of two mixed phases in CC-CCH@CMO.[19]

2.2. The Electrochemical Properties of the CC-ZnO@C-Zn and CC-CCH@CMO Flexible Electrodes

The formation of dendrites on the anode is usually inevitable in Zn-based batteries especially with the increased number of cycles, owing to the inhomogeneous distribution of current and electrode corrosion during the electrochemical reaction.[20] Here, in order to demonstrate the role of our well-crafted anode in suppressing the dendrite growth, scanning electron microscopy (SEM) images of the CC-ZnO@C-Zn anode or the

Zn plate (both using CC-CCH@CMO as the cathode) after different cycles were investigated. When the Zn plate was used as the anode, the SEM images show obvious dendrite formation after 1000 cycles at 40 mA cm^{-2} (**Figure 2**a). The corresponding elemental mappings display an increased O content originating from the ZnO formed as the dead Zn during cycling. In contrast, the CC-ZnO@C-Zn anode exhibits excellent properties in inhibiting the Zn dendrite growth even after 1500 cycles (Figure 2b). Furthermore, the XRD pattern of the CC-ZnO@C-Zn anode after cycling indicates that the peaks are well indexed to metal zinc after cycling despite a little Zn(OH)$_2$ appearing. As a comparison, the XRD pattern of the Zn plate shows obvious peaks of low conductivity ZnO as the dead Zn (due to the irreversible reaction Zn(OH)$_2$ → ZnO+H$_2$O) after 1000 cycles. This kind of dead Zn greatly shortens the battery life, resulting in a low capacity retention of 63.7% (Figure S12, Supporting Information). As illustrated in Figure 2e, the Zn plate can be corroded during the discharging process (Zn + 4OH$^-$ → Zn(OH)$_4^{2-}$ + 2e^-), which results in the bulges and concaves on the surface of Zn plate. Then, the charges would preferentially gather on the bulges, leading to an increased practical current density on the bulges and eventually the formation of
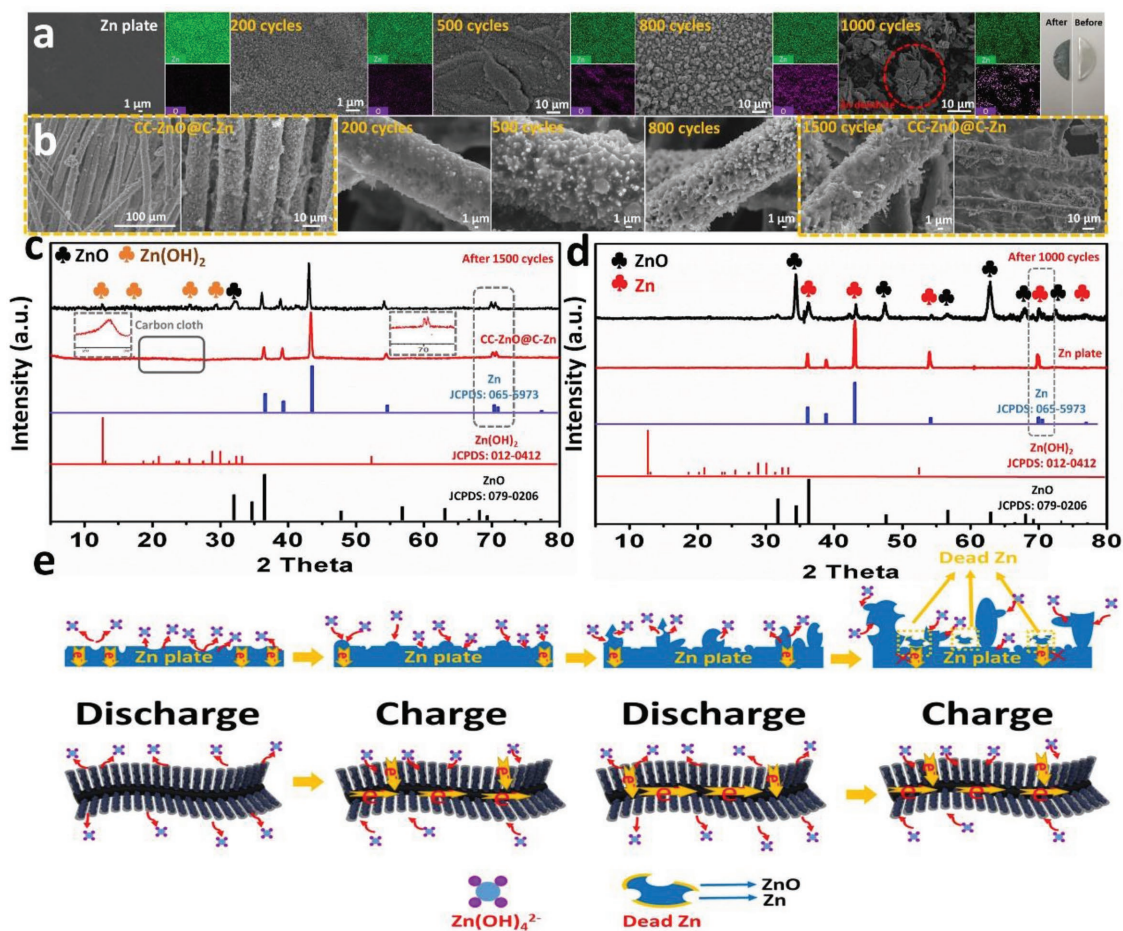

Figure 2. a) SEM and the corresponding elemental mapping images of the Zn plate during cycling when Zn plate is used as anode in Zn–Co battery. b) SEM images of CC-ZnO@C-Zn during cycling in our Zn-Co battery. Ex situ XRD patterns of c) CC-ZnO@C-Zn, and d) Zn plate anode before and after cycles. e) Schematic illustration of the dendrite formation mechanism on the Zn plate and the antidendrite mechanism for the CC-ZnO@C-Zn anode.

dendrites. By contrast, the finely crafted skeleton can effectively avoid this kind of situation and inhibit the Zn dendrite formation by enabling a uniform charge distribution and providing fast and effective electron transfer channels (Figure 2e). On the other hand, the Zn deposition processes on the CC-ZnO@C and on the CC were compared by studying the current–time (*i–t*) curves at a constant cathodic overpotential (η = −0.2 V). As shown in Figure S13 (Supporting Information), the CC-ZnO@C exhibits a stable current density while the CC shows a much increased current density due to the dramatic growth of dendrites, further demonstrating the antidendrite property of the CC-ZnO@C electrode by allowing uniform Zn deposition, which is confirmed by the SEM images.[21] In brief, the 3D ZnO@C skeleton matrix plays an important role from four aspects: 1) It enables the uniform charge distribution on the electrode, and avoids charges being concentrated on local regions. 2) It provides fast electron transfer channels and so increases the effective contact area between the electrode and the electrolyte. 3) It allows a uniform Zn deposition by

anchoring the deposited Zn layer and so effectively avoids the shedding of Zn from carbon cloth.[22]

To investigate the electrochemical properties of the finely crafted flexible 3D electrodes, the CC-ZnO@C-Zn and CC-CCH@CMO electrodes were tested separately in a three-electrode system. For the CC-ZnO@C-Zn electrode, the cyclic voltammetry (CV) curves show a similar shape and an increased CV area when the scan rate increases from 10 to 30 mV s^{-1}, with a pair of redox peaks (−1.5 V, −1.2 V vs Hg/HgO) observed, corresponding to the reversible Zn^{2+}/Zn redox process ($Zn + 4OH^- \leftrightarrows Zn(OH)_4^{2-} + 2e^-$) (**Figure 3**a).[23] Its redox potential is obviously lower than that of other anode materials such as carbon (≈−1 V),[24] iron oxide (≈−1.2 V)[25] and Bi (≈−1 V),[26] implying that a high output voltage would be expected when used as the anode of a full battery. Moreover, the CC-ZnO@C-Zn containing 3D skeleton displays a small resistance like the Zn plate (Figure S14, Supporting Information). The Tafel curves were employed to further study the effect of carbon coating on the corrosion behavior (Figure 3b). Apparently, the corrosion
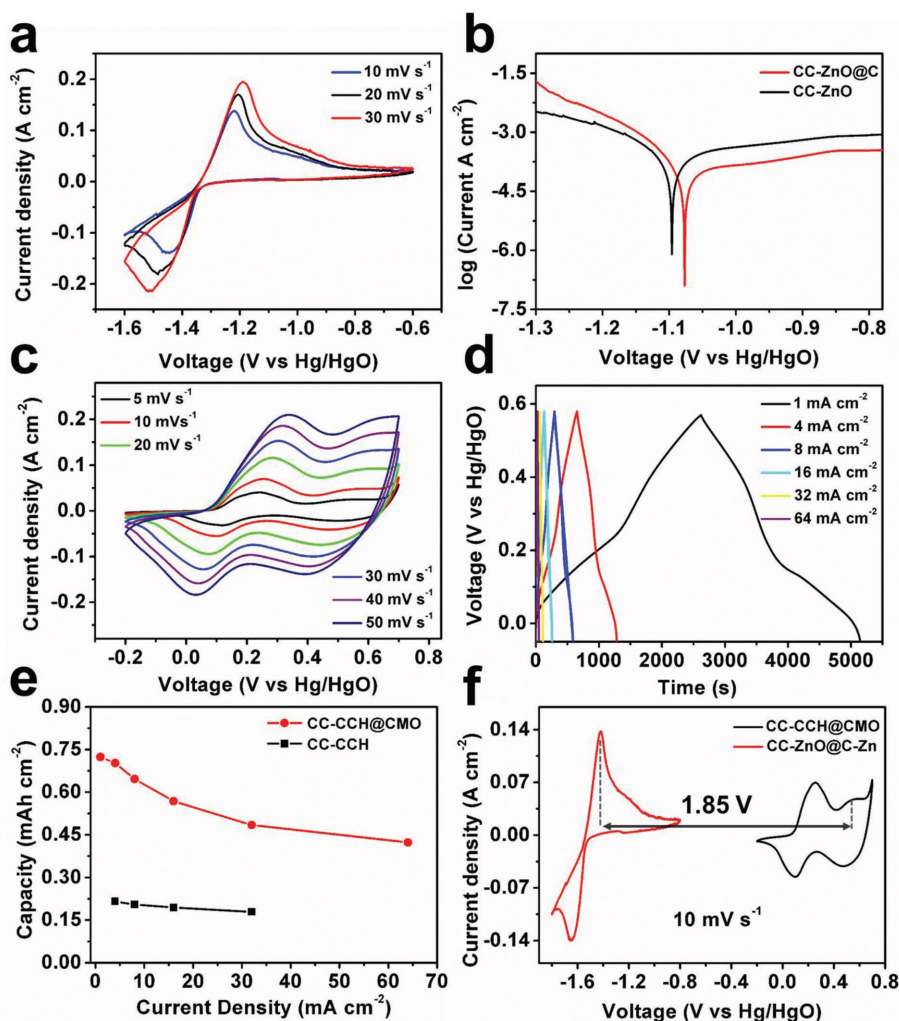

Figure 3. a) CV curves of CC-ZnO@C-Zn at different scan rates. b) Tafel plot curves of CC-ZnO@C and CC-ZnO. c) CV and d) charge–discharge curves of CC-CCH@CMO. e) Areal capacity values at different current densities of CC-CCH@CMO and CC-CCH. f) A comparison of CV curves for the CC-ZnO@C-Zn and the CC-CCH@CMO electrodes at a scan rate of 10 mV s^{-1}.
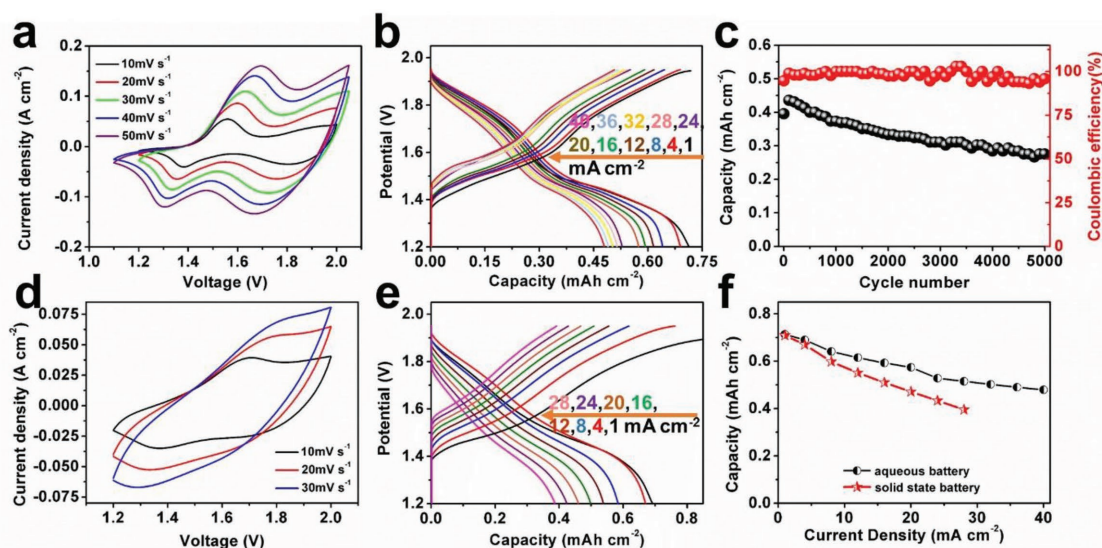
**ADVANCED
SCIENCE NEWS**
www.advancedsciencenews.com

**ADVANCED
FUNCTIONAL
MATERIALS**
www.afm-journal.de

Figure 4. a) CV curves, b) galvanostatic charge–discharge curves and c) long-term cycling performance and corresponding Coulombic efficiency of the aqueous Zn–Co battery at a current density of 80 mA cm^{-2}. d) CV curves and e) galvanostatic charge–discharge curves of the all-solid-state Zn–Co battery. f) Comparison of the rate performance for the aqueous Zn–Co battery and the all-solid-state Zn–Co battery.

current of CC-ZnO@C decreases and the corrosion potential exhibits a positive shift (from −1.1 to −1.08 V) compared to the CC-ZnO, implying an improved anti-corrosion property for the carbon-coated ZnO (CC-ZnO@C). It can be attributed to the protective carbon coating which decreases the direct contact of ZnO and electrolyte.[27] For the CC-CCH@CMO electrode, CV curves show two pairs of redox peaks (Figure 3c), which can be assigned to the following electrochemical reactions: $Co^{2+} + 3OH^- \leftrightarrows CoOOH + H_2O + e^-$; $CoOOH + OH^- \leftrightarrows CoO_2 + H_2O + e^{-}$[28] and also match well with the charge–discharge platforms in Figure 3d. The CC-CCH@CMO electrode delivers a high specific areal capacity of 0.72 mAh cm^{-2} (260.2 mAh g^{-1}) at a current density of 1 mA cm^{-2} (0.36 A g^{-1}), which is higher than that for most of previously reported Co-based materials.[29] Even though at a high current density of 64 mA cm^{-2} (23.02 A g^{-1}), the capacity still maintains 0.42 mAh cm^{-2} (152.2 mAh g^{-1}), holding a high capacity retention of 67.6% (Figure 3e). In contrast, the CC-CCH material exhibits much lower specific areal capacities of only 0.21–0.18 mAh cm^{-2} at various current densities of 4-32 mA cm^{-2} (Figure S15a,b, Supporting Information). The increased capacity can be attributed to the enhanced conductivity of CC-CCH@CMO (Figure S15c, Supporting Information) originating from the finely crafted 3D heterostructure and the synergetic effect between CCH and CMO.[30] Moreover, the CV curves of CC-ZnO@C-Zn and CC-CCH@CMO at 10 mV s^{-1} (Figure 3f) show a large redox potential separation (1.85 V) between the anode material and the cathode material, indicating a high expected output voltage for the Zn–Co battery in this work.

2.3. Electrochemical Properties of Zn–Co Full Battery

On the basis of the excellent electrochemical performance of the anode and cathode materials, an aqueous Zn-Co battery

was assembled using 3D hierarchical CC-ZnO@C-Zn as the anode and CC-CCH@CMO as the cathode. In **Figure 4**a, the CV curves show two pairs of redox peaks with a symmetrical shape at various scan rates, demonstrating the highly reversible redox reaction of the Zn–Co battery in aqueous electrolyte. As depicted in Figure 4b, the charge–discharge curves indicate a significant high output voltage (1.75 V), which is consistent with our expectation. It is higher than the output voltage of other types of aqueous batteries, such as Zn–Mn batteries (1.2–1.4 V),[31] Ni–Fe batteries (1.1–1.2 V),[32] and Zn ion battery (0.3–0.65 V).[33] In particular, the voltage hysteresis between the discharge platform (1.75, 1.45 V) and the charge platform (1.85, 1.55 V) is only ≈0.1 V (Figure 4b), indicating fast redox processes. Based on the charge–discharge curves, the maximum capacity was 0.71 mAh cm^{-2} at 1 mA cm^{-2}. When the current density was increased to 40 mA cm^{-2}, a high capacity of 0.48 mAh cm^{-2} still retained. Notably, an ultrafast charge process lasts only 45 s in such a situation, much faster than most of ordinary Ni–Zn batteries.[11] In contrast, the Zn–Co battery using CC-CCH as the cathode (without CoMoO$_4$) exhibits apparent inferior performances (Figure S16a,b, Supporting Information) with a much lower maximum capacity of only 0.20 mAh cm^{-2} at 4 mA cm^{-2} compared to the CC-CCH@CMO cathode system.

The long-term cycling performances of the Zn–Co battery were investigated at different current densities. Benefiting from the antidendrite properties of the 3D hierarchical CC-ZnO@C-Zn anode, this Zn–Co battery exhibits a very high capacity retention of 71.1% over 5000 cycles at 80 mA cm^{-2} as well as an almost 100% Coulombic efficiency (Figure 4c). The charging–discharging curves show little change during the whole process (Figure S17, Supporting Information). The enhanced cycling performance is attributed to the 3D skeleton in the anode which effectively suppresses the formation of dendrites. In detail, 93.3% and 80% of the initial capacity are retained at the first 1000 and 3000 cycles, respectively. Even when the current

ADVANCED
SCIENCE NEWS
www.advancedsciencenews.com

ADVANCED
FUNCTIONAL
MATERIALS
www.afm-journal.de

density is decreased to 40 mA cm^{-2}, a good capacity retention of 82.5% over 1500 cycles could also be obtained, demonstrating the ultrastable cycling performances (Figure S18, Supporting Information) which is consistent with the well-maintained morphology after long-term cycling observed in the SEM images of Figure 2b. In particular, the 3D skeleton obtained by flushing the cycled electrodes several times further shows the excellent stability after the cycling process (Figure S19, Supporting Information). As a comparison, a Zn–Co battery was also assembled using the CC-Zn anode and the CC-CCH@CMO cathode, which displays an obvious capacity fading after 500 cycles. This is caused by the loss of Zn from the carbon cloth without the anchoring of skeletons (Figure S20 and inset, Supporting Information).

An all-solid-state Zn–Co battery was also assembled using the same anode and cathode together with the PVA–KOH gel electrolyte. In Figure 4d, the CV curves show the analogous shape compared to the Zn–Co battery using the aqueous electrolyte at different scan rates but exhibit less obvious redox peaks. The charge–discharge plots display two discharge platforms at 1.8 V and 1.5 V with a slight voltage increase of ≈0.05 V compared to the aqueous Zn–Co battery, which can be attributed to the higher electron transfer resistance of the gel electrolyte (Figure S21, Supporting Information).[34] Impressively, a high capacity of 0.70 mAh cm^{-2} was achieved at 1 mA cm^{-2}, which is almost

equivalent to the capacity obtained in the aqueous electrolyte (Figure 4e). Even at a high current density of 28 mA cm^{-2}, the capacity of 0.39 mAh cm^{-2} still remains. Although at higher current densities, the solid-state battery shows slightly lower capacities than that of the aqueous battery (≈67.6%), the capacity retention is as high as ≈55.7% (all solid state), implying the excellent rate performance of the solid-state Zn–Co battery (Figure 4f).

2.4. Electrochemical Properties of Fiber-Shaped Zn–Co Battery

In view of the excellent electrochemical performances demonstrated above, an all-solid-state flexible fiber-shaped Zn–Co battery was assembled (**Figure 5**a). The fiber-shaped battery displays typical CV curves with two pairs of redox peaks at slow scan rates but broadened curves with the scan rate increasing (Figure 5b). According to the discharge curves (based on the whole volume of fiber-shaped battery), the maximum capacity is up to 3 mAh cm^{-3} at 25 mA cm^{-3} (Figure 5c). The capacity retention is 82% after 1600 cycles (Figure 5d) at 250 mA cm^{-3}, exhibiting an excellent cycling stability. To further demonstrate the flexibility of our fiber-shaped battery, a series of deformation tests were carried out at 125 mA cm^{-3} under various deformation states (Figure 5e). The discharge curves are highly similar
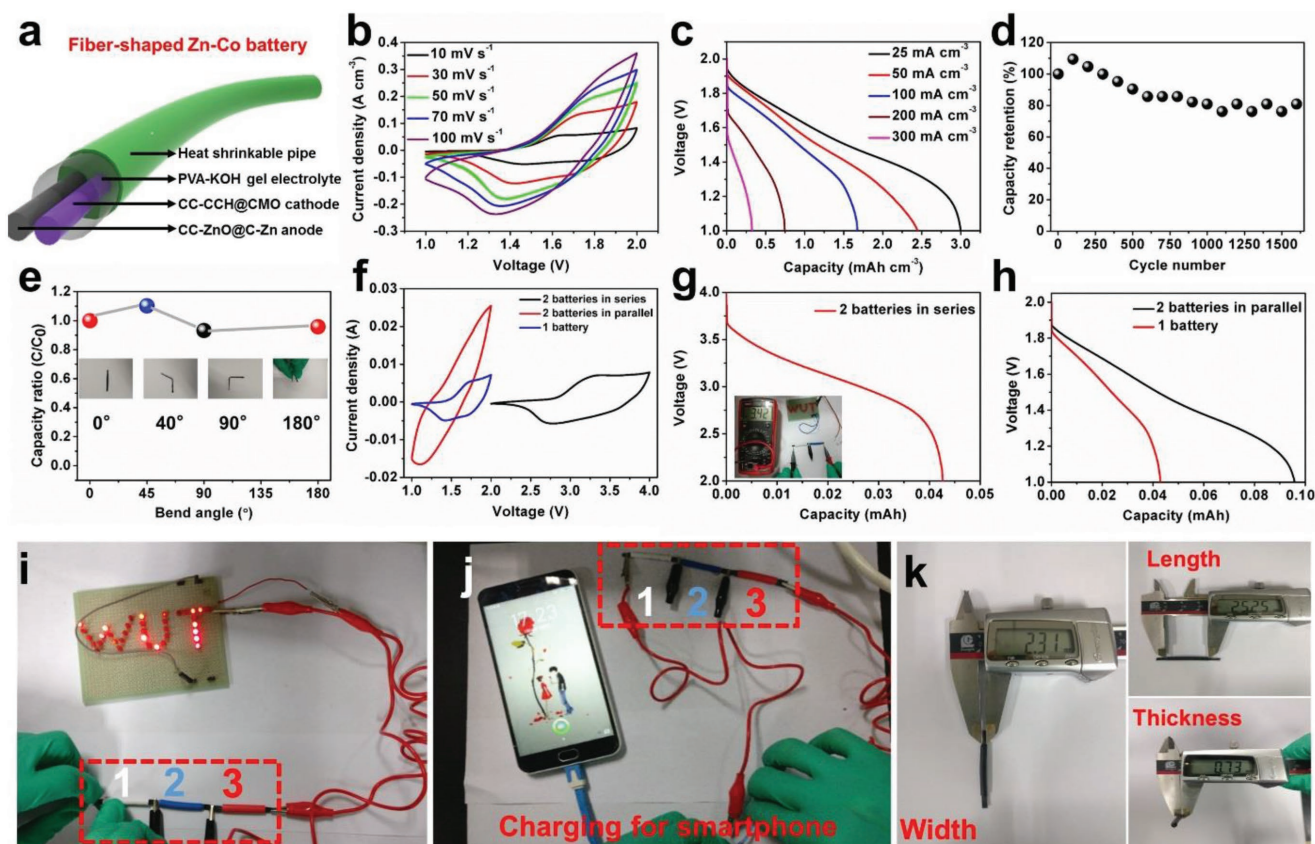

Figure 5. a) Schematics of the all-solid-state fiber-shaped Zn–Co battery. b) CV curves, c) galvanostatic discharge curves, and d) cycling performance of the all-solid-state fiber-shaped Zn–Co battery at a current density of 250 mA cm^{-3}. e) Capacity ratios at various deformation states. f) CV curves and g,h) galvanostatic discharge curves of in-series and in-parallel batteries. The inset in (g) is the typical voltage output of the two-in-series battery. i, j) A series of LEDs and a smartphone were powered by three-in-series battery. k) The digital photos of a single fiber-shaped Zn–Co battery.

with a minimal capacity variation at different bending degrees (Figure S22, Supporting Information). The flexible battery also exhibits excellent performances under a number of bending tests with a 92.5% capacity retention over 100 times of bending (Figure S23, Supporting Information). In particular, benefiting from the unique fiber shape, the flexible battery can be arranged to a variety of configurations to meet different needs. Therefore, a customizable flexible wire-shaped device with a wide voltage window or high capacity can be obtained by several batteries in series or in parallel. As shown in Figure 5f,g, a wire-based device was achieved by two-series-connected battery and displayed a wide voltage window (2–4 V). In like manner, three-in-series battery further showed a threefold window (2–6 V) and held the high output voltage (Figure S24, Supporting Information). Moreover, a wire-based device with a twofold capacity was also obtained by two-in-parallel battery (Figure 5f,h). Hence, by increasing the number of batteries in series or parallel, the voltage window or capacity of flexible device can be continuously expanded. As shown in Figure 5i,j, a wire-shaped flexible device consisting of three batteries in series was used to successfully power a series of LEDs and was also capable of charging a smartphone. The fiber-shaped device can also be weaved as a bracelet to power a digital watch (Figure S25, Supporting Information). The volume of a single battery unit was calculated by measuring the length, width and thickness with a vernier caliper (Figure 5k). In principle, our tailor-made devices with a variety of different capacities and voltage windows can be further assembled to power different electronics, which indicates the great potential of our fiber-shaped battery in real applications.

The Zn–Co battery exhibits high energy/power densities of 235 Wh kg^{-1}/12.6 kW kg^{-1} (aqueous state) and 221.9 Wh kg^{-1}/10.6 kW kg^{-1} (solid state) based on the total mass of active materials on both electrodes. These values are higher than most other previously reported aqueous batteries (**Figure 6**a and Table S1, Supporting Information). Additionally, the maximum energy density based on the volume of our fiber-shaped Zn–Co battery (2.31 mm × 25.25 mm × 0.73 mm) is further calculated in Figure 6b. The peak energy density of 4.6 mWh cm^{-3} together with a maximum power density of 0.42 W cm^{-3} are also higher than those in the recent reports on flexible

energy storage devices (Table S2, Supporting Information), implying the excellent electrochemical performances of our fiber-shaped battery.

3. Conclusion

In summary, a dendrite-free and long-durability (71.1% after 5000 cycles) Zn–Co battery with high energy/power densities (235 Wh kg^{-1}, 12.6 kW kg^{-1}) has been developed. The 3D trilayer CC-ZnO@C-Zn anode exhibited excellent antidendrite property due to the finely crafted skeleton of core-shell CC-ZnO@C nanorod arrays, while the 3D hierarchical branch-like CC-CCH@CMO cathode contributes to its high capacity. Furthermore, a flexible fiber-shaped all-solid-state Zn–Co battery using the gel electrolyte was assembled for the first time. It presents superior performances, including long cycling (82% capacity retention after 1600 cycles) and high energy/power densities (4.6 mWh cm^{-3}, 0.42 W cm^{-3}). In particular, the fiber shape of our Zn–Co battery enables it to be easily customized to meet different needs for portable electronics such as a series of LEDs, a smartphone and a digital watch. Our work demonstrates an innovative way to achieve flexible high-performance Zn–Co batteries, which show great potentials in the applications of flexible and portable electronics.

4. Experimental Section

Synthesis of CC-ZnO: Prior to the synthesis procedure, the CC was soaked in concentrated nitric acid overnight, then washed with deionized water and alcohol several times to remove the residual acid, and finally the CC was dried in a vacuum oven at 70 °C. Then, the CC (WOS1002, 2 cm × 2.5 cm) was dipped into KMnO$_4$ (0.5 M) about 30 min for surface treatment and washed with deionized water several times to remove the residual KMnO$_4$. The ZnO nanorods were in situ grown on CC by a simple hydrothermal process. Briefly, Zn(NO$_3$)$_2$·6H$_2$O (3.12 g), and hexamethylenetetramine (1.47 g) were dissolved in deionized water (50 mL). The ammonia (5.25 mL) was added to adjust the pH to about 11. After magnetic stirring for 30 min, the obtained transparent solution was transferred into a Teflon-lined stainless-steel autoclave (100 mL) containing the pretreated CC. The autoclave was sealed and hydrothermally treated at 90 °C for 24 h to obtain the CC-ZnO. The
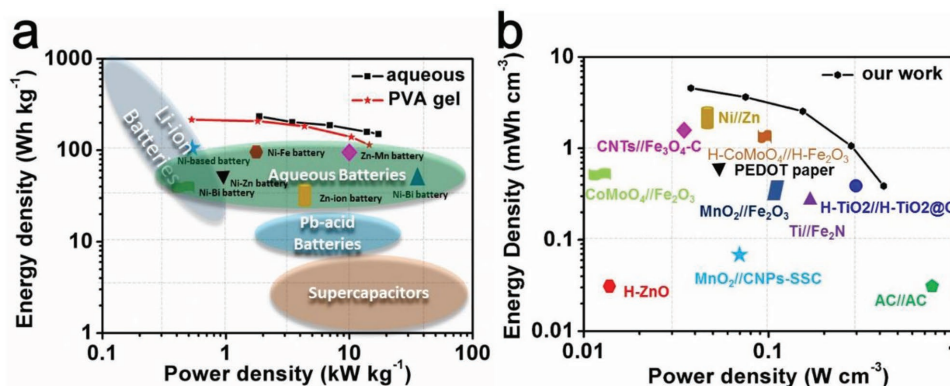

Figure 6. a) Ragone plot of the aqueous Zn–Co full battery and the all-solid-state Zn–Co battery using PVA gel as the electrolyte with the energy density calculated based on the mass of active materials on both electrodes. b) Ragone plot of the all-solid-state fiber-shaped Zn–Co battery based on the volume of the whole flexible battery.

sample was then taken out and rinsed several times in deionized water before being dried in an oven at 70 °C.

Synthesis of the 3D CC-ZnO@C Skeleton: The as-prepared ZnO nanorod arrays on CC (2 cm × 2.5 cm), 2-methylimidazole (3 g) were placed in a glass dish and heated at 150 °C under low-pressure conditions in a vacuum oven (≈100 Pa). After being treated at 650 °C in N_2 gas for 3 h, the 3D CC-ZnO@C was obtained. The mass loading of the 3D skeleton is 5.4 mg cm^{-2}.

Synthesis of the CC-ZnO@C-Zn Anode: A Pt plate and Hg/HgO were used as the counter electrode and the reference electrode, respectively. The metallic Zn was deposited via the electrodeposition method in the electrolyte containing 6 M KOH with 1.5 M ZnO, using CC-ZnO@C as the working electrode. The electrodeposition of Zn was easily carried out by continuously charging at −1.6 V for 10 min at current density of 15 mA cm^{-2} and the trilayer CC-ZnO@C-Zn anode was obtained, the mass loading of Zn is 2.2 mg cm^{-2}.

Synthesis of CC-CCH: $CoCl_2 \cdot 6H_2O$ (5 mmol), urea (10 mmol), and NH_4F (4 mmol) were dissolved in deionized water (50 mL) under constant magnetic stirring for a few minutes to form a pink solution. The solution containing a piece of pretreated CC (drop a few drops of alcohol on the CC to improve the hydrophilicity) was then transferred to a Teflon-lined stainless-steel autoclave (100 mL). The autoclave was sealed and maintained at 120 °C for 12 h and then cooled to room temperature. After the sample was taken out, it was rinsed several times with deionized water and dried in an oven at 70 °C to obtain CC-CCH. The mass loading of the sample is 1 mg cm^{-2}.

Synthesis of CC-CCH@CMO: $CoCl_2 \cdot 6H_2O$ (0.14 g) and $Na_2MoO_4 \cdot 2H_2O$ (0.15 g) were dissolved in deionized water (50 mL) under constant magnetic stirring. Then, the solution was transferred into a Teflon-lined stainless-steel autoclave (100 mL) already containing the as-prepared CC-CCH and maintained at 180 °C for 10 h. After cooling to room temperature, the 3D branch-like CC-CCH@CMO was removed from the Teflon and dried at 70 °C after rinsing with distilled water and then cooled to room temperature. The mass loading of the sample is 2.78 mg cm^{-2}.

Materials Characterization: To observe the morphology, SEM (and EDS)/TEM (and HRTEM) were performed with JEOL JSM-7100F scanning electron microscope and JEM-2100F/Titan G2 60-300 transmission electron microscope. X-ray diffractometer characterizations were carried out with a D8 Discover X-ray diffractometer with nonmonochromated Cu Kα X-ray source (λ = 1.054056 Å). Raman spectrum was acquired using a Renishaw INVIA micro-Raman spectroscopy system. Fourier transform-infrared (FTIR) transmittance spectra were measured using a Nicolet 60-SXB IR spectrometer. XPS measurements were performed using a VG MultiLab 2000 instrument. The mass of the electrodes was also recorded by an AX/MX/UMX Balance (METTLER TOLEDO, maximum = 5.1 g; delta = 0.001 mg).

Electrochemical Characterization: The electrochemical measurements were conducted using a CHI 760E Electrochemical Workstation (CH Instruments, China) at room temperature. The current–time (i–t) curves were undertaken by a three-electrode configuration at a constant cathodic overpotential (η = −0.2 V), using CC or CC-ZnO@C-Zn as the working electrode, Hg/HgO as the reference electrode, Pt plate as the counter electrode, 6 M KOH with 1.5 M ZnO solution as the electrolyte. For three-electrode system tests, CC-ZnO@C-Zn anode or CC-CMO cathode were directly used as the working electrode without any metal support or current collector. A Pt plate and an Hg/HgO were used as the counter electrode and the reference electrode, respectively. 6 M KOH with 1.5 M ZnO solution was used as electrolyte. For the assembly of the Zn–Co battery, CC-ZnO@C-Zn and CC-CCH@CMO were directly used for anode and cathode simultaneously in a two-electrode system. The all-solid-state electrolyte (6 M KOH-PVA) was prepared as follows: First, 3 g PVA was dissolved in deionized water (30 mL) and stirred at 85 °C for 3 h until the solution became transparent. Afterward, 6 M KOH with 1.5 M ZnO solution (9 mL) was added drop by drop and stirred evenly to obtain gel electrolyte, then two electrodes were soaked in the gel electrolyte (acts as both the electrolyte and the separator). The electrodes were allowed to solidify under ambient conditions for 3 h

before they were assembled face to face and packaged by heat shrink tube. Herein, the PVA–KOH gel was used as electrolyte and separator. The specific capacity of the electrode was calculated according to the formula: $C = It/B$, I is discharge current, t is discharge time, and B is area of electrode or mass of active materials (based on cathode). The energy density (E) and power density (P) of the full battery were calculated using the formulas: $E = \int_0^t IV(t)dt/A$, $P = E/t$, I is discharge current, A is mass of active materials or the whole volume of fiber-shaped device, V is discharge voltage and t is discharge time. EIS measurements were carried out by applying an AC voltage with 5 mV amplitude in a frequency range from 0.01 Hz to 100 kHz at open circuit potential.

Supporting Information

Supporting Information is available from the Wiley Online Library or from the author.

Acknowledgements

Conflict of Interest

The authors declare no conflict of interest.

Keywords

[1] a) W. Liu, M. S. Song, B. Kong, Y. Cui, *Adv. Mater.* **2017**, *29*, 1603436; b) Y. Huang, W. S. Ip, Y. Y. Lau, J. Sun, J. Zeng, Y. Nss, W. S. Ng, H. Li, Z. Pei, Q. Xue, *ACS Nano* **2017**, *11*, 8953.

[2] a) Z. Cai, L. Xu, M. Yan, C. Han, L. He, K. M. Hercule, C. Niu, Z. Yuan, W. Xu, L. Qu, K. Zhao, L. Mai, *Nano Lett.* **2015**, *15*, 738; b) H. Chang, H. Wu, *Energy Environ. Sci.* **2013**, *6*, 3483; c) Z. Yao, X. Xia, C. A. Zhou, Y. Zhong, Y. Wang, S. Deng, W. Wang, X. Wang, J. Tu, *Adv. Sci.* **2018**, *5*, 1700786; d) J. Zhan, S. Deng, Y. Zhong, Y. Wang, X. Wang, Y. Yu, X. Xia, J. Tu, *Nano Energy* **2018**, *44*, 265; e) Y. Zhong, X. Xia, S. Deng, J. Zhan, R. Fang, Y. Xia, X. Wang, Q. Zhang, J. Tu, *Adv. Energy Mater.* **2018**, *8*, 1701110; f) Q. Chen, S. Sun, T. Zhai, M. Yang, X. Zhao, H. Xia, *Adv. Energy Mater.* **2018**, 201800054.

[3] J. Liu, K. Song, P. A. van Aken, J. Maier, Y. Yu, *Nano Lett.* **2014**, *14*, 2597.

[4] a) J. Bae, M. K. Song, Y. J. Park, J. M. Kim, M. Liu, Z. L. Wang, *Angew. Chem. Int. Ed.* **2011**, *50*, 1683; b) C. Zhu, P. Yang, D. Chao,

X. Wang, X. Zhang, S. Chen, B. K. Tay, H. Huang, H. Zhang, W. Mai, *Adv. Mater.* **2015**, *27*, 4566.

[5] P. Simon, Y. Gogotsi, *Nat. Mater.* **2008**, *7*, 845.

[6] K. Watanabe, T. Kikuoka, N. Kumagai, *J. Appl. Electrochem.* **1995**, *25*, 219.

[7] a) G. Wang, L. Fu, N. Zhao, L. Yang, Y. Wu, H. Wu, *Angew. Chem. Int. Ed.* **2007**, *46*, 295; b) D. U. Lee, J. Fu, M. G. Park, H. Liu, K. A. Ghorbani, Z. Chen, *Nano Lett.* **2016**, *16*, 1794.

[8] a) J. W. Diggle, A. R. Despic, J. O. M. Bockris, *J. Electrochem. Soc.* **1969**, *116*, 5; b) A. P. Pavlov, L. K. Grigorieva, S. P. Chizhik, V. K. Stankov, *J. Power Sources* **1996**, *62*, 113; c) B. Yang, Z. Yang, R. Wang, *J. Power Sources* **2014**, *251*, 14.

[9] S. H. Lee, C. W. Yi, K. Kim, *J. Phys. Chem. C* **2011**, *115*, 2572.

[10] a) Y. F. Yuan, J. P. Tu, H. M. Wu, Y. Li, D. Q. Shi, X. B. Zhao, *J. Power Sources* **2006**, *159*, 357; b) Y. F. Yuan, J. P. Tu, H. M. Wu, Y. Z. Yang, D. Q. Shi, X. B. Zhao, *Electrochim. Acta* **2006**, *51*, 3632; c) R. Wen, Z. Yang, X. Fan, Z. Tan, B. Yang, *Electrochim. Acta* **2012**, *83*, 376; d) J. Huang, Z. Yang, R. Wang, Z. Zhang, Z. Feng, X. Xie, *J. Mater. Chem. A* **2015**, *3*, 7429.

[11] J. Liu, C. Guan, C. Zhou, Z. Fan, Q. Ke, G. Zhang, C. Liu, J. Wang, *Adv. Mater.* **2016**, *28*, 8732.

[12] T. Wang, Z. Yang, J. Huang, R. Wang, Z. Zhao, *Electrochim. Acta* **2013**, *112*, 104.

[13] J. Meng, X. Liu, J. Li, Q. Li, C. Zhao, L. Xu, X. Wang, F. Liu, W. Yang, X. Xu, Z. Liu, C. Niu, L. Mai, *Nano Lett.* **2017**, *17*, 7773.

[14] J. Yang, F. Zhang, H. Lu, X. Hong, H. Jiang, Y. Wu, Y. Li, *Angew. Chem. Int. Ed.* **2015**, *127*, 11039.

[15] G. Zhang, S. Hou, H. Zhang, W. Zeng, F. Yan, C. C. Li, H. Duan, *Adv. Mater.* **2015**, *27*, 2400.

[16] J. Meng, C. Niu, L. Xu, J. Li, X. Liu, X. Wang, Y. Wu, X. Xu, W. Chen, Q. Li, Z. Zhu, D. Zhao, L. Mai, *J. Am. Chem. Soc.* **2017**, *139*, 8212.

[17] A. C. Ferrari, J. Robertson, *Phys. Rev. B: Condens. Matter* **2000**, *61*, 14095.

[18] Y. Li, H. Wang, J. Jian, Y. Fan, L. Yu, G. Cheng, J. Zhou, M. Sun, *RSC Adv.* **2016**, *6*, 13957.

[19] M. Q. Yu, L. X. Jiang, H. G. Yang, *Chem. Commun.* **2015**, *51*, 14361.

[20] K. Fukami, S. Nakanishi, H. Yamasaki, T. Tada, K. Sonoda, N. Kamikawa, N. Tsuji, H. Sakaguchi, Y. Nakato, *J. Phys. Chem. C* **2007**, *111*, 1150.

[21] C. J. Lan, C. Y. Lee, T. S. Chin, *Electrochim. Acta* **2007**, *52*, 5407.

[22] Y. Zhong, D. Chao, S. Deng, J. Zhan, R. Fang, Y. Xia, Y. Wang, X. Wang, X. Xia, J. Tu, *Adv. Funct. Mater.* **2018**, 1706391.

[23] J. F. Parker, C. N. Chervin, I. R. Pala, M. Machler, M. F. Burz, J. W. Long, D. R. Rolison, *Science* **2017**, *356*, 415.

[24] L. Sheng, L. Jiang, T. Wei, Z. Liu, Z. Fan, *Adv. Energy Mater.* **2017**, *7*, 1700668.

[25] a) Y. Li, J. Xu, T. Feng, Q. Yao, J. Xie, H. Xia, *Adv. Funct. Mater.* **2017**, *27*, 1606728; b) K. A. Owusu, L. Qu, J. Li, Z. Wang, K. Zhao, C. Yang, K. M. Hercule, C. Lin, C. Shi, Q. Wei, *Nat. Commun.* **2017**, *8*, 14264.

[26] Y. Zeng, Z. Lin, Y. Meng, Y. Wang, M. Yu, X. Lu, Y. Tong, *Adv. Mater.* **2016**, *28*, 9188.

[27] a) J. Li, T. Zhao, E. Shangguan, Y. Li, L. Li, D. Wang, M. Wang, Z. Chang, Q. Li, *Electrochim. Acta* **2017**, *236*, 180; b) X. Fan, Z. Yang, W. Long, B. Yang, J. Jing, R. Wang, *Electrochim. Acta* **2013**, *108*, 741.

[28] a) Y. Zheng, Z. Li, J. Xu, T. Wang, X. Liu, X. Duan, Y. Ma, Y. Zhou, C. Pei, *Nano Energy* **2015**, *20*, 94; b) T. Zhai, L. Wan, S. Sun, Q. Chen, J. Sun, Q. Xia, H. Xia, *Adv. Mater.* **2017**, *29*, 1604167.

[29] a) C. Yuan, L. Yang, L. Hou, L. Shen, X. Zhang, X. W. Lou, *Energy Environ. Sci.* **2012**, *5*, 7883; b) L. Wang, Z. H. Dong, Z. G. Wang, F. X. Zhang, J. Jin, *Adv. Funct. Mater.* **2013**, *23*, 2758.

[30] A. Izadi-Najafabadi, D. N. Futaba, S. Iijima, K. Hata, *J. Am. Chem. Soc.* **2010**, *132*, 18017.

[31] a) W. Sun, F. Wang, S. Hou, C. Yang, X. Fan, Z. Ma, T. Gao, F. Han, R. Hu, M. Zhu, C. Wang, *J. Am. Chem. Soc.* **2017**, *139*, 9775; b) Y. Zeng, X. Zhang, Y. Meng, M. Yu, J. Yi, Y. Wu, X. Lu, Y. Tong, *Adv. Mater.* **2017**, *29*, 1700274; c) C. Xu, B. Li, H. Du, F. Kang, *Angew. Chem. Int. Ed.* **2012**, *51*, 933.

[32] a) J. Liu, M. Chen, L. Zhang, J. Jiang, J. Yan, Y. Huang, J. Lin, H. J. Fan, Z. X. Shen, *Nano Lett.* **2014**, *14*, 7180; b) C. Guan, W. Zhao, Y. Hu, Q. Ke, X. Li, H. Zhang, J. Wang, *Adv. Energy Mater.* **2016**, *6*, 1601034.

[33] a) P. He, M. Yan, G. Zhang, R. Sun, L. Chen, Q. An, L. Mai, *Adv. Energy Mater.* **2017**, *7*, 1601920; b) W. Kaveevivitchai, A. Manthiram, *J. Mater. Chem. A* **2016**, *4*, 18737.

[34] A. A. Mohamad, N. S. Mohamed, M. Z. A. Yahya, R. Othman, S. Ramesh, Y. Alias, A. K. Arof, *Solid State Ionics* **2003**, *156*, 171.